Published in final edited form as:
Anal Chem. 2011 January 15; 83(2): 542–548. doi:10.1021/ac102113v.

Equilibrium and Kinetic Behavior of $Fe(CN)_6^{3-/4-}$ and Cytochrome c in Direct Electrochemistry Using a Film Electrode Thin-Layer Transmission Cell

Yingrui Dai[a], **Yi Zheng**[b], **Greg M. Swain**[a], and **Denis A. Proshlyakov**[a,*]

[a]Department of Chemistry, Michigan State University, East Lansing, MI 48824-1322

[b]Department of Microbiology and Molecular Genetics, Michigan State University, East Lansing, MI 48824-1322

Abstract

We report on the design and performance of a thin-layer electrochemical cell optimized for use with optically transparent film electrodes in combination with UV/Vis and IR transmission spectroscopic measurements. The cell allows for measurements under both aerobic and anaerobic conditions. The direct, unmediated electron transfer, as assessed by the current transient, and the corresponding optical response observed for the $Fe(CN)_6^{3-/4-}$ couple were in good agreement with theoretical predictions for voltammetry and optical absorption by an analyte confined in a thin layer. Chronoamperometric and spectroscopic measurements of $Fe(CN)_6^{3-/4-}$ on gold mesh electrode revealed fast kinetics strongly influenced by the electrolyte concentration. Maximal apparent rates exceeding 2 s^{-1} in 1 M KCl were observed optically. The direct kinetic and thermodynamic behavior of cytochrome *c* was compared with several electrode materials using the cell. The results showed heme ligand-dependent changes in the protein-electrode interactions. Mid-UV/Visible spectral changes upon redox transitions in native cytochrome *c* and its cyanide derivative, as well as dissociation of the ferrous cytochrome *c* - CN complex are reported.

INTRODUCTION

Spectroelectrochemistry is a powerful hybrid technique that provides quantitative and qualitative information about an analyte by combining spectroscopy (*e.g.*, UV to far-IR transmission) with electrochemical methods. A thin-layer electrochemical (TLE) cell, and its optically transparent variant, has become an essential tool in the study of complex redox reaction mechanisms, especially in biological systems.[1-9] Development and utilization of optically transparent electrodes (OTE) opens particularly intriguing possibilities in the rapidly developing area of interfacial assemblies by allowing one to manipulate and monitor the sample directly on the solid surface. Examples of such assemblies include partially dehydrated protein films,[10-13] supported lipid bilayers,[14, 15] protein/lipid films,[14, 16-19] and surface-immobilized protein assemblies.[20-22] This approach holds great promise for other bioanalytical applications and sensors.[22-24] However, there are significant practical limitations on physical properties of the electrode and the geometry of sample in current implementations of TLE cells. This is especially true for transmission studies, as electrochemical performance is often sacrificed for optical transmission.

* To whom correspondence should be addressed. proshlya@msu.edu..

The configuration and performance of a TLE cell depends strongly on the selection of electrode material (film electrode *vs.* minigrid, for example), which determines minimal ohmic resistance/maximal geometry of the cell, available potential and spectral window. These factors, in turn, determine attainable electron-transfer rates, sample type, stability, etc. A gold minigrid (Au-MG) is a commonly used OTE due to its availability, transmission from the far-UV to the far-IR spectral region, and high conductivity.[1, 7-9] While the opaque nature of metals has been overcome by use of reflectance measurements, other limitations (narrow potential window, background current, protein fouling) remain.[25]

A thin conductive film supported on an optically transparent substrate represents another type of OTE with a broad analytical potential. Depending on the spectral region of interest, conductive thin films, such as metals,[26, 27] carbon materials,[5, 28-32] and metal oxides,[33-35] are used. Usually, a compromise between the electrical conductivity and optical transparency has to be made as these two parameters are inversely related to one another, and both of which are controlled by film thickness.[36]

An ideal TLE cell should satisfy several criteria: a) rapid and complete electrolysis of the redox analyte, and b) quantitative agreement between the experimental and theoretical optical and electrochemical parameters. From practical standpoint the cell also needs to c) accept a flexible range of electrode materials, including film electrodes, d) require small operational sample volume, including anaerobic conditions, and e) provide reproducible, quantitative portability between optical and infrared domains (physically and spectrally) for direct spectral correlations.

We sought to achieve these key benchmarks with particular emphasis on (i) faster electron-transfer kinetics (exceeding the typical 20-120 sec time frame)[32, 37] and (ii) compatibility with optically transparent diamond electrodes for interfacial protein spectroelectrochemistry. We have previously reported application of this cell in IR transmission measurements of ferricyanide and ferrocene using boron-doped diamond (BDD) on silica.[38] Herein, we report on the extensive characterization of the spectral and electrochemical response of ferricyanide, cytochrome *c* (C*c*) and its cyanide derivative (C*c*-CN) in aqueous media using the new cell design along with several electrode materials. Using a potential step/ spectrophotometric approach, we report redox- and ligand-dependent changes in the rates of electrochemical reactions and assess anaerobic performance.

MATERIALS AND METHODS

Thin-Layer Spectroelectrochemical Cell

The transmission TLE cell design (Figure 1) builds upon an original design by Mantelle *et. al.*[7] but with significant modifications which greatly increased the responsiveness, predictability and reliability of the cell. The optically transparent working electrode (20×20 mm overall, 10 mm dia. active area) is pressed against the front surface of the cell body (PEEK) though a circular Kapton® polyimide film spacer (Fig. 1). The inner diameter of the spacer (10 mm) is larger than that of the central through bore of the cell (9 mm) except for three small tabs that extended into the bore by ~1 mm. A transparent back window (9 mm dia. × 5 mm) - CaF_2 (used here), BaF_2, Si, fused silica etc. - was pressed against the electrode through the spacer tabs by a hollow nut on the back surface of the window. Thus, the electrochemical volume of the cell is defined by the narrow space between two flat surfaces separated by the spacer of the desired thickness (7.5 to 75 μm) and the I.D. of the spacer. This volume is sealed with one o-ring encircling the spacer (Fig. 1, bottom) and another between the perimeter of the non-electrochemical surface of the back window and the hollow nut (not shown). A circular contact of smallest possible diameter (17 mm) is pressed against the working electrode outside of the front o-ring (WE lead in Fig. 1).

Approximately ~10 cm of fine Pt wire serves as the counter electrode. It is either located in a 1×1 mm groove in cell body encircling the back window (shown in Fig. 1, top) or coiled in a separate compartment that is connected to that groove through a PEEK frit (1.5 mm dia.). The latter configuration provides better separation between the sample and the counter electrode medium at the expense of small increase in ohmic resistance. Continuity in the electric circuit between the electrochemical cavity and the counter electrode is established via a cylindrical capillary volume (EC in Fig. 1; ~50 μm wide) filled with supporting electrolyte. Capillary is formed by the outer cylindrical surface of the back window and the inner surface of central bore. For aqueous measurements, the cell is equipped with a miniature standard Ag/AgCl reference electrode. The reference electrode is connected to the side of the cylindrical capillary between the working and counter electrodes via a cracked glass junction.

Utilization of the capillary electrolyte space surrounding the optical transmission window for circuit continuity allowed to minimize the dimensions of the thin layer in the plane of the electrode. At the same time this configuration a) made the cell fully compatible with a wide range of electrode materials and geometries, particularly with film electrodes on non-conductive substrates, and b) allowed to use a film spacers with desired thickness (7.5 to 75 μm used here) to predictably define the thickness of electrochemical layer. An integral miniature reference Ag/AgCl electrode was used in this highly compact configuration (25 × 35 × 50 mm). For further details of cell design and methods of preparation of optically transparent boron-doped diamond thin film, glassy carbon, and gold minigrid electrodes see SI.

Chemicals

All chemicals were reagent grade quality, or better, and were used without additional purification. A solution of $K_3Fe(CN)_6$ (Aldrich) was prepared fresh daily using ultrapure water (~18 MΩ cm) from a commercial water purification system (Barnstead E-pure). Horse heart cytochrome *c* (Sigma Aldrich Chemical Co.) was re-purified chromatographically and concentrated following a published procedure[39] in 10 mM Tris-HCl buffer, pH 7. Cc concentrations were determined using $\Delta\varepsilon_{550} = 21\ cm^{-1}\ mM^{-1}$ in the ferro- vs. ferri-C*c* difference spectrum. For CN^--modified C*c*, a small aliquot of stock KCN solution was added to the final concentration of 0.1 M and pre-incubated for 30 min prior to the experiment.

Electrochemistry and UV-Vis Measurements

The electrochemical measurements were performed at room temperature using a computer-controlled potentiostat (Model 760B, CH Instruments, Inc., Austin, TX). All potentials are reported vs. a Ag/AgCl reference electrode. Background voltammetric scans obtained using a blank sample immediately before or after the measurements were subtracted from those of the sample. For chronoamperometric measurements, no background correction was performed. UV-Vis spectra were recorded continuously at 0.3 s intervals using Hewlett Packard 8453 diode array spectrophotometer (Agilent Technologies, Santa Clara, CA). Optical spectra were probed in the central area of the electrode (~6 mm dia.) as shown in Fig. 1B. The start of the optical and amperometric measurements was electronically synchronized. The apparent electron-transfer rates upon application of the potential step were determined by a non-linear regression analysis of optical transient at characteristic wavelengths, fitting with a mono- or bi-exponential functions using Igor Pro software (Wavemetrics, Inc., Lake Oswego, OR).

For aerobic measurements, the analyte solution is loaded by placing a small volume of sample (5-10 μL) in the center of working electrode immediately prior to the assembly of

the cell otherwise filled with the supporting electrolyte. Anaerobic performance of the cell was evaluated using ferro-myoglobin as a sensitive probe the presence of traces of oxygen.[40] There were no indications of O_2 binding to Mb^{2+} sample in the cell upon incubation in the dark over 12 h. Details of anaerobic sample handling and representative spectroelectrochemical optical spectra are shown in SI.

RESULTS

Equilibrium electrochemical performance of the cell

Symmetric oxidation and reduction peaks are observed in the background-corrected cyclic voltammetric *i-E* curves for $Fe(CN)_6^{4-}$ in 1 M KCl at a glassy carbon electrode with no evidence of any diffusional tailing (Fig. 2A). The i_p^{ox} / i_p^{red} and Q_p^{ox} / Q_p^{red} ratios of 0.99±0.04 and 1.01±0.06 (n > 200), respectively, are indicative of exhaustive electrolysis. The $E_{½}$ values for $Fe(CN)_6^{3-/4-}$ were stable under all conditions ($E_{½}$ = 286±3 mV).

Average quantitative parameters obtained from the *i-E* curves illustrated in Fig. 2A are summarized in Fig. 2B for a range of conditions. To facilitate comparison of current and charge obtained under a wide range of conditions, the corresponding average values (n ≥ 3) were normalized to the amount of analyte per thin layer area, *i.e.*, concentration × thickness. Such normalization emphasizes deviation from ideal values and allows to directly compare amplitudes occurring at the low and high ends of concentration and layer thickness ranges. This approach simplifies determination of the limitations in electrochemical behavior as compared to direct analysis of raw values, which are provided in SI.

The normalized peak current (i_N) in thin layer voltammetry is expected to rise with scan rate and remain constant with concentration. Such ideal behavior was observed for the 25 and 75 μm spacers, while i_N for the 7.5 μm spacer was significantly higher (Fig. 2B, left). Disproportionally high i_N with the 7.5 μm spacer was particularly noticeable at lower scan rates and the relative difference diminished at higher scan rates. For the 25 and 75 μm spacers, i_N remained constant with $Fe(CN)_6^{4-}$ concentration. Some decrease in i_N was observed for the 7.5 μm spacer at low analyte concentrations. This apparent decrease is likely to be due to an increase in experimental error when peak current decreases significantly below background current under these conditions.

The normalized charge (Q_N) was similar for the 25 and 75 μm spacers and remained constant with analyte concentration (Fig. 2B, center). No significant change was observed in Q_N at scan rates ≥5 mV/s but some increase was observed at lower scan rates, particularly with the 25 μm spacer. Similar to i_N, Q_N was significantly higher for the 7.5 μm spacer than for 25 and 75 μm spacers and it was further increased at low scan rates. The apparent thickness of the electroactive sample layer calculated from Q_N was in good agreement with the theoretical values obtained from thickness of 75 and 25 μm spacers and corresponding optical absorption measurements. Actual layer thickness obtained optically for 7.5 μm spacer correlated with the theoretical value as well, however corresponding Q_N was significantly larger than expected for this spacer (see SI for details).

The peak potential separation (ΔE_p) increased with increasing scan rate for all spacer thicknesses used here (Fig. 2B, right). Higher sample concentrations had little effect on ΔE_p with 25 μm and 75 μm spacers at low scan rates (1-2 mV/s), indicative of near-equilibrium conditions. The increase in ΔE_p with a 1 mM sample concentration at scan rates (10-20 mV/s) can be attributed to the increasing effect of ohmic resistance with the rise in peak current. The ΔE_p was the lowest with the 25 μm spacer and remained below the 59 mV predicted for an n=1 diffusion-controlled redox reaction under all conditions. No clear concentration

dependence was observed for 7.5 μm spacer, but at low scan rates the ΔE_p was significantly higher than with the other spacers .

Spectroelectrochemical Assessment of the Reaction Rates

The time dependence of the faradaic current, *i*, and UV optical absorption, *A*, for the oxidation of $Fe(CN)_6^{4-}$ at a Au-MG electrode is shown in Figure 3A. The faradaic current is a direct measure of the reaction *rate* while the optical absorption is proportional to the *amount* of reactant that absorbs light. Thus, the *A*-*t* curves were converted into derivative form for direct comparison with simultaneously acquired amperometric data. In the 0.1 M supporting electrolyte, the maximal apparent rate of electrolysis $Fe(CN)_6^{3-/4-}$ was observed at 1 and 4 s in the $\Delta A/\Delta t$ curves for the 1 and 5 mM concentrations, respectively. With 1 M supporting electrolyte most of the electrolysis occurred within instrument sampling time (0.3 sec). In both cases, the maximal rate of optical changes probed in the central part of the electrode (as shown in Fig. 1) correlated with the slowest amperometric phase. The initial, optically silent amperometric phase is attributed to the charging of the double layer and electrolysis in the peripheral, dark areas of the cavity.

Optical changes associated with the reduction of C*c* during the double potential step are shown in Figure 4A. Since the cell configuration and conditions for the protein measurement were the same as in Figure 3, the ohmic resistance was similar in both cases. The apparent rate of reduction and oxidation of C*c* was determined from the temporal changes between peak and trough in the difference absorption spectrum. The observed rate constant (k=0.14 s^{-1}, Fig. 4A, solid markers) was lower than that for 1 mM $Fe(CN)_6^{3-/4-}$ (Fig. 3A) in spite of a 10x lower concentration in the case of C*c*, although the rate constant could be somewhat underestimated due to a 3x larger layer thickness for C*c*. Significantly slower kinetics (k=0.02 s^{-1}) was observed for the reduction and oxidation of the protein on BDD (Fig. 4A, open markers). Considering that the experimental conditions were otherwise identical for the BDD and Au-MG electrodes, the difference in the observed kinetics is attributed entirely to the ohmic resistance of the electrode and/or its interactions with C*c* (see discussion).

Stable and fully reversible spectral changes for C*c* were observed upon repetitive potential steps between on BDD over tens of minutes with no degradation of the electrochemical response (Fig. 4B). While electrochemical kinetics for C*c* on Au-MG was relatively fast at the beginning, both the rates and amplitudes of spectral changes diminished noticeably with time (Fig. 4B). Approximately a 50% decrease in the rate of each successive cycle was observed for Au-MG comparing to 10% decrease for BDD in spite of >5x longer cycles in the latter case. As the results, kinetics on Au-MG became slower than on BDD after 10-15 min of redox cycling. Changes in electrochemical kinetics involved a semi-permanent modification of the electrode surface since the reaction rates were not recovered upon loading of a fresh C*c* sample until the electrode was regenerated by acid washing and cysteamine modification.

Redox difference spectra of Cytochrome *c*

Stable, reproducible, and fully reversible spectra were observed for C*c* with BDD electrode (Fig. 5) while the amplitude of spectral changes gradually decreased in the case of Au-MG electrode. Characteristic absorption maxima and clear isosbestic points associated with the reduction of C*c* were observed throughout visible region. An absorption maximum was observed at 315 nm with isosbestic points at 288 and 338 nm. Optical stability and the absence of mediators allowed us to record well-defined, reversible redox-difference transitions below 260 nm. Two maxima were observed at 204 and 236 nm with Au-MG electrode and the trough at ~220 nm. The 236 nm transition was also clearly seen with BDD, although light absorption below ~225 nm due to the band gap transition of the electrode

partially obscures the high-energy transition in C*c*. These features are consistent with the circular dichroic spectra of C*c* in the 200-260 nm region.[41] The spectral region around the 280 nm protein absorption maximum showed no evidence of redox-sensitive electronic transitions originating from the heme in agreement with the reported spectra of C*c* in vacuum.

Taking advantage of the chemical resistance BDD affords, we examined redox-difference optical absorption spectra of the C*c*-CN complex (Fig. 5B) where exogenous cyanide is bound to heme iron displacing the Met_{80} residue as a ligand. The $E^{o\prime}$ of C*c*-$CN^{2+/3+}$ was reported to be -0.44 V vs. Ag/AgCl electrode.[42] To monitor only the reduction of C*c*-CN complex sample was pre-incubated at -0.3 V until optical changes were complete. Reduction of native C*c* (cyanide-free, $E^{o\prime}$= +0.06V vs. Ag/AgCl) during pre-incubation yielded difference spectra nearly identical to those in Fig. 5A with the amplitude of approximately 15% of that for native C*c*. Although somewhat larger than predicted for simple binding of cyanide to Fe^{3+}-C*c* under conditions used in this study (K_D^{ox}=5 mM)[43] and applied potential of -0.3 V is expected to shift this equilibrium toward ligand-free protein (see below).

Significantly different optical changes were observed upon subsequent reduction. Transition arising from ferric (negative) and ferrous (positive) forms in the visible spectrum were shifted by 4-6 nm to lower energy. The near-UV transition at 316 nm was essentially unchanged from the native C*c* suggesting that it is sensitive to the oxidation state, but not to the nature of the axial ligand. The 236-nm transition of the native C*c* was either absent or shifted to significantly higher energy in the C*c*-CN complex suggesting that this transition may involve Met_{80} ligand. The 220-290 nm spectral region was featureless in this complex.

At -0.7 V, the C*c*-CN complex ($E - E^{o\prime}$ = -0.26 V) was reduced with an apparent rate of k=0.13 s^{-1}. Reduction of the native C*c* at -0.3 V was significantly slower (0.05 s^{-1}) in spite of a larger overpotential ($E - E^{o\prime}$ = -0.36 V). Rapid reduction of C*c*-CN was followed by additional slow optical changes with an apparent rate of k=0.014 s^{-1} (Fig. 5B, inset). This phase was associated with distinctly different optical changes than those observed upon reduction C*c* or C*c*-CN (Fig. 5C). Three symmetrical shifts to a higher energy were observed in the visible spectrum at 411/423, 518/519, and 549/557 nm. These spectral features were fully consistent with the difference between Cc^{2+} and Cc^{2+}-CN expected from the spectra shown in Figs. 4A and 4B and thus were assigned to the dissociation of CN^- ligand from the Cc^{2+}-CN complex.[44] The rate of dissociation observed here is comparable to the earlier study involving chemical reduction of Cc^{3+}-CN^-.[45] Little changes were observed around 315 nm upon CN^- dissociation in agreement with spectral similarity between $Cc^{3+/2+}$ and $Cc^{3+/2+}$-CN^- in this region. A new transition was observed at 230 nm, although its reversibility could not be confirmed directly due to irreversible dissociation of CN^- from ferrous C*c* (K_D^{red}=213 M).[42] The presence of electronic transition at 230 nm can be expected from comparison of redox-difference spectra of C*c* and C*c*-CN.

A ~3x faster reduction of the C*c*-CN^- complex shows that the rate of reduction of native C*c* is not limited by the ohmic resistance of BDD. Therefore the difference in the electrochemical rates of C*c* on BDD and Au-MG electrodes is attributed to C*c* interactions with positively charged amine groups of modified Au or relatively hydrophobic surface of BDD.

DISCUSSION

Responsiveness of the thin-layer transmission cell

The maximal apparent rate of a redox reaction can be limited by three factors: analyte diffusion, the overall conductivity of the cell, and the intrinsic heterogeneous electron transfer rate constant. The effective ohmic resistance at the optically active center of the layer is determined by the geometry of the electrode and resistivities of both the electrode film and the solution above. The relative contribution of the film electrode to the overall ohmic resistance increases with increasing thickness of the sample layer (TL, Fig. 1) as the amount of analyte increases and the resistance of thin layer decreases. On the other hand, the thickness of the analyte layer determines the maximal diffusion-limited reaction rate and the spectral pathlength (water absorption in IR, minimal detectable analyte concentration *etc*.).

Our results show that the rate of optical changes for $Fe(CN)_6^{4-}$ on Au-MG tracks the final amperometric phase (Fig. 3) and scales with the electrolyte concentration. Since ohmic resistance of Au-MG is negligible and the intrinsic rate of electron transfer on the electrode is constant between experiments, changes in the apparent rates seen in Fig. 3 represent the maximal attainable redox rates as limited by the ohmic resistance of the electrolyte. Therefore, any apparent rates slower than those in Fig. 3 at corresponding electrolyte concentration can only be determined by the intrinsic rate of reduction/oxidation, ohmic resistance of the electrode, and, in some cases, analyte diffusion. Differentiation between these factors has to be done on case-by-case basis as illustrated below. Yet faster response can be easily achieved in smaller cells but further size reduction has spectroscopic drawbacks: high power density of probe light increases photoreactions (Fig. 6),[46, 47] while a small diameter IR beam decreases throughput and increases noise.

The key difference between the metal grid and film electrodes involves transparency of electrode material. Light transmitted through the film electrode can probe analyte at the electrode/electrolyte interface thus allowing for spectroscopic studies on direct electron transfer. While significantly more demanding in terms of cell design, BDD electrodes offer several major benefits in analytical applications: an outstanding chemical inertness, stability, as illustrated in Fig. 5, and wide potential window.[38, 48-52] Ohmic resistance of film OTE, including BDD) has to be balanced against optical transmission determined by film thickness and doping, but small surface charge and background current of BDD can offset the effect of their ohmic resistance to some extent. The TLE cell described here exhibits nearly-ideal behavior in most conditions with two notable exceptions related to the diffusion limit as described in SI. Additional studies are currently under way to overcome these limitations and to develop composite film electrodes with low ohmic resistance that will allow yet faster spectroelectrochemical measurements.

Electrochemcial Spectroscopy and Kinetics of Cytochrome *c*

Potential step measurements on $Fe(CN)_6^{4-}$ allowed us to evaluate the maximal observable rate at given concentration of the supporting electrolyte as determined by cell geometry. Under restrictive experimental conditions, required for most biological application (*i.e.*, 100 mM KCl and <1 mM analyte), electrochemcial processes with rates of 1 s^{-1} can be well resolved.

Apparent reaction rates of C*c* were significantly slower than reactions of $Fe(CN)_6^{4-}$ under same conditions and thus represent the rate of absorption/desorption on the electrode and intrinsic rate of electron transfer. The rates of reduction and oxidation of native C*c* at comparable overpotentials were similar. Since both rates were significantly slower on BDD comparing to Au-MG, one could argue that kinetics was limited by the ohmic resistance of BDD film. However, a 2.5-fold faster rate was observed for the reduction C*c*-CN^- complex

in spite of a smaller overpotential than for C*c*. This clearly indicates that the kinetics of native C*c* is not limited by the cell and must be attributed to the interactions between C*c* and BDD. Similarity in the rate of reduction and oxidation of native C*c* is not unexpected considering its structural rigidity and physiological role as an electron carrier. The origin of facile electron transfer in the C*c*-CN^- complex is not clear at present, but it is likely that dissociation of the axial Met_{80} ligand upon binding of CN^- increases structural flexibility of the protein[53] and either allows for great exposure of hydrophobic residues, thus stabilizing interaction with a generally hydrophobic BDD, or increases exposure of the heme macrocycle and permits its closer approach to the electrode.

The B (~400 nm) and Q (~550 nm) π-π* transitions in the spectrum of a heme involve dipole matrix elements of the entire macrocyle[54] and thus substitution of nitrogen in C*c*-CN for sulfur in the native C*c* is expected to cause optical shifts in this region (Fig. 5). Higher energy transitions, such as N- and L- bands between 300 and 360 nm, involve primarily individual pyrrole rings and are less sensitive to the axial ligation. This assignment is supported by the spectral similarity in the 290-375 nm region between $Cc^{2+/3+}$ and $Cc^{2+/3+}$-CN redox differences, as well as featureless difference spectrum upon dissociation of Cc^{2+}-CN (Fig. 5C). The transition around 200 nm (Fig. 5A) likely originates from the M-band reported at 200 nm for model iron porphyrins in vacuum[55] and is not expected to be ligand-sensitive. Interestingly, the 236-nm transition is either absent or shifted to higher energy in the C*c*-CN complex. The loss of absorption at this wavelength in d^{10} metal complex of Mb^{2+} and its sensitivity to CN^- binding suggests that it is associated with the S-Fe^{3+} ligation, although it is too intense ($\Delta\varepsilon = 6\ mM^{-1}\ cm^{-1}$) to be directly assigned to the charge transfer transition.[56] The 240-300 nm region where most amino-acid radical species[57] and all aromatic residues[40] absorb light is relatively clear from porphyrin absorption providing an important spectral window for studies on these species without spectral interference from the heme.

CONCLUSIONS

The configuration of the thin-layer transmission electrochemical cell reported here provides an optimum balance between rapid spectroelectrochemical response, predictable and reproducible quantitative parameters, and broad flexibility in selection of electrode materials. The maximal rate of electrolysis is primarily determined by the concentration of the supporting electrolyte and the ohmic resistance of the working electrode allowing one to achieve optical response in sub-second timescales. Application of the cell to protein measurements with boron-doped diamond film yielded a stable, reversible optical response over several hours with little electrode fouling and tight control over gas atmosphere. We report spectroscopic and kinetics characterization of the direct electrochemistry of native and cyanide-modified cytochrome *c*.

Supplementary Material

Refer to Web version on PubMed Central for supplementary material.

Acknowledgments

This research was sponsored by grants from the National Science Foundation (Grant CHE-0911383, G.M.S.) and the National Institutes of Health (Grant GM 070544, D.A.P.).

REFERENCES

1. Berthomieu C, Marboutin L, Dupeyrat F, Bouyer P. Biopolymers. 2006; 82:363–367. [PubMed: 16453337]

2. Kuwana T, Darlington KR, Leedy DW. Anal. Chem. 1964; 36:2023–2025.
3. Anderson JL, Kuwana T, Hartzell CR. Biochemistry. 1976; 15:3847–3855. [PubMed: 182219]
4. Bowden EF, Hawkridge FM. Journal of Electroanalytical Chemistry. 1981; 125:367–386.
5. Zak J, Porter MD, Kuwana T. Anal. Chem. 1983; 55:2219–2222.
6. Gui Y, Kuwana T. Journal of Electroanalytical Chemistry. 1987; 226:199–209.
7. Moss D, Nabedryk E, Breton J, Mantele W. Eur. J. Biochem. 1990; 187:565–572. [PubMed: 2154376]
8. Schlereth DD, Mantele W. Biochemistry. 1992; 31:7494–7502. [PubMed: 1510936]
9. Marboutin L, Desbois A, Berthomieu C. J Phys Chem B. 2009; 113:4492–4499. [PubMed: 19320527]
10. Rich PR, Breton J. Biochemistry. 2002; 41:967–973. [PubMed: 11790120]
11. Iwaki M, Breton J, Rich PR. Biochimica et Biophysica Acta (BBA) -Bioenergetics. 2002; 1555:116–121.
12. Iwaki M, Giotta L, Akinsiku AO, Schagger H, Fisher N, Breton J, Rich PR. Biochemistry. 2003; 42:11109–11119. [PubMed: 14503861]
13. Marshall D, Rich PR. Method Enzymol. 2009; 456:53–74.
14. Santos HA, Garcia-Morales V, Pereira CM. Chemphyschem. 2010; 11:28–41. [PubMed: 19943272]
15. Brzozowska M, Oberts BP, Blanchard GJ, Majewski J, Krysinski P. Langmuir. 2009; 25:9337–9345. [PubMed: 19518134]
16. Rusling JF, Nassar A-EF. J. Am. Chem. Soc. 1993; 115:11891–11897.
17. Nassar AEF, Willis WS, Rusling JF. Anal. Chem. 1995; 67:2386–2392. [PubMed: 8686876]
18. Rusling JF. Acc. Chem. Res. 1998; 31:363–369.
19. Jeuken LJ. Nat Prod Rep. 2009; 26:1234–1240. [PubMed: 19779638]
20. Wu Y, Hu S. Bioelectrochemistry. 2006; 68:105–112. [PubMed: 16043421]
21. Yue H, Waldeck DH, Petrovic J, Clark RA. J. Phys. Chem. B. 2006; 110:5062–5072. [PubMed: 16526749]
22. Caseli L, Crespilho FN, Nobre TM, Zaniquelli MED, Zucolotto V, Oliveira ON. J. Colloid Interface Sci. 2008; 319:100–108. [PubMed: 18093610]
23. Grieshaber D, MacKenzie R, Voros J, Reimhult E. Sensors. 2008; 8:1400–1458.
24. Chen D, Li JH. Surf. Sci. Rep. 2006; 61:445–463.
25. Bernad S, Mantele W. Analytical Biochemistry. 2006; 351:214–218. [PubMed: 16530718]
26. Yildiz A, Kissinger PT, Reilley CN. Anal. Chem. 1968; 40:1018–1024.
27. Benken, W. v.; Kuwana, T. Anal. Chem. 1970; 42:1114–1116.
28. DeAngelis TP, Hurst RW, Yacynych AM, Mark HB Jr. Wllliam R H, Mattson JS. Anal. Chem. 1977; 49:1395–1398.
29. Sorrels JW, Dewald HD. Anal. Chem. 1990; 62:1640–1643.
30. Anjo DM, Brown S, Wang L. Anal. Chem. 1993; 65:317–319. [PubMed: 8447620]
31. Donner S, Li H-W, Yeung ES, Porter MD. Analytical Chemistry. 2006; 78:2816–2822. [PubMed: 16615798]
32. Dai Y, Swain G, Porter MD, Zak J. Analytical Chemistry. 2008; 80:14–22. [PubMed: 18260192]
33. Armstrong NR, Lin AWC, Fujihira M, Kuwana T. Anal. Chem. 1976; 48:741–750.
34. Ginley DS, Bright C. MRS Bull. 2000; 25:15–18.
35. Donley C, Dunphy D, Paine D, Carter C, Nebesny K, Lee P, Alloway D, Armstrong NR. Langmuir. 2002; 18:450–457.
36. Haacke G. Annual Review of Materials Science. 1977; 7:73–93.
37. Haymond S, Zak JK, Show Y, Butler JE, Babcock GT, Swain GM. Anal. Chim. Acta. 2003; 500:137–144.
38. Dai Y, Proshlyakov DA, Zak JK, Swain GM. Analytical Chemistry. 2007; 79:7526–7533. [PubMed: 17784734]

39. Brautigan DL, Ferguson-Miller S, Margoliash E. Journal of Biological Chemistry. 1978; 253:130–139. [PubMed: 201614]
40. Grzyska PK, Hausinger RP, Proshlyakov DA. Anal Biochem. 2010; 399:64–71. [PubMed: 19932076]
41. Flatmark T. J Biol Chem. 1967; 242:2454–2459. [PubMed: 6026235]
42. Schejter A, Ryan MD, Blizzard ER, Zhang C, Margoliash E, Feinberg BA. Protein Science. 2006; 15:234–241. [PubMed: 16434742]
43. George P, Tsou CL. Biochem J. 1952; 50:440–448. [PubMed: 14925115]
44. Butt WD, Keilin D. P Roy Soc Lond B Bio. 1962; 156:429–&.
45. George P, Schejter A. J Biol Chem. 1964; 239:1504–1508. [PubMed: 14189884]
46. Paul P, Kumta US. Radiat Res. 1973; 56:238–245. [PubMed: 4749590]
47. Lee Y, Song KB. J Biochem Mol Biol. 2002; 35:590–594. [PubMed: 12470593]
48. Xu J, Granger MC, Chen Q, Strojek JW, Lister TE, Swain GM. Anal. Chem. 1997; 69:591A–597A.
49. Swain GM, Anderson AB, Angus JC. MRS Bulletin. 1998; 23:56–59.
50. Rao TN, Loo BH, Sarada BV, Terashima C, Fujishima A. Anal. Chem. 2002; 74:1578–1583. [PubMed: 12033247]
51. Fujishima A, Rao TN, Try DA. Proc.-Electrochem. Soc. 2000; 99-32:383–388.
52. McGaw EA, Swain GM. Analytica Chimica Acta. 2006; 575:180–189. [PubMed: 17723589]
53. de Jongh HH, Goormaghtigh E, Ruysschaert JM. Biochemistry. 1995; 34:172–179. [PubMed: 7819193]
54. Baerends EJ, Ricciardi G, Rosa A, van Gisbergen SJA. Coordin Chem Rev. 2002; 230:5–27.
55. Edwards L, Dolphin DH, Gouterma M. J Mol Spectrosc. 1970; 35:90–109.
56. Verbaro D, Hagarman A, Soffer J, Schweitzer-Stenner R. Biochemistry. 2009; 48:2990–2996. [PubMed: 19222214]
57. Proshlyakov DA. Biochim Biophys Acta. 2004; 1655:282–289. [PubMed: 15100043]

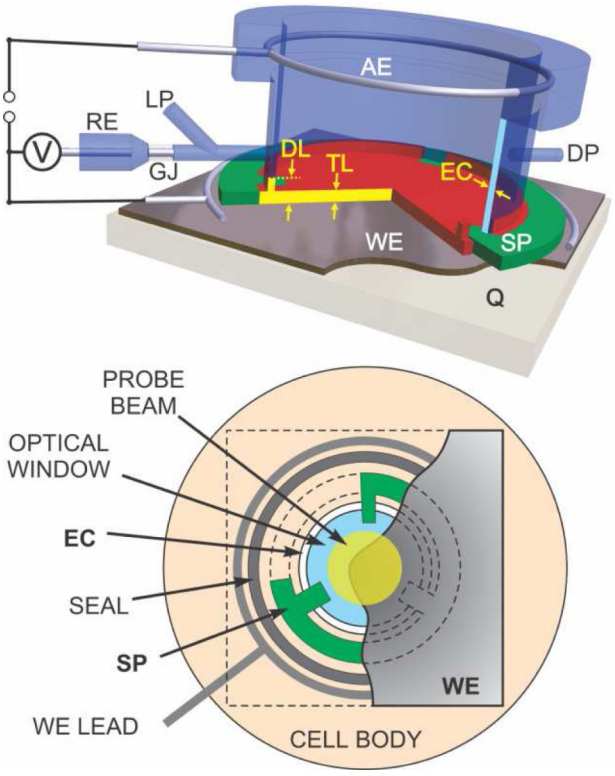

Figure 1.

Diagram of the film electrode transmission thin-layer spectroelectrochemical cell. The thin layer (TL) is formed between the working electrode (WE) and the optical transmission window. The thickness of TL is determined by the spacer (SP). BDD, metal minigrid, or other thin film electrodes are supported by optically transparent substrate (Q). The thin layer is connected to the auxiliary electrode (AE) via electrolyte capillary (EC) between the optical window and outer cell body. Electric contact with WE is provided by a circular wire or foil lead outside of the cell cavity. Reference measurement is provided by a miniature Ag/AgCl electrode (RE) via cracked glass junction (GJ). Reference electrode capillary is also used as a sample loading port (LP), which is exhausted via a similar discharge port (DP) on the opposite side. Part of electrolyte capillary up to the diffusion limit (DL) from working electrode can be electrochemically active. Bottom diagram shows schematic view from the side of working electrode (cutout) along the probe beam path. The width of electrolyte capillary (EC) is exaggerated for clarity.

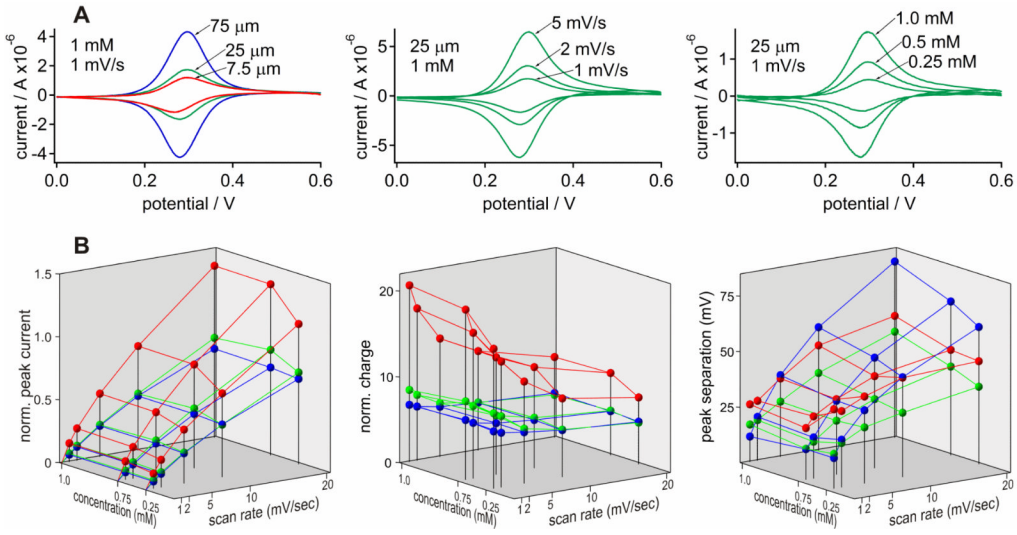

Figure 2.

Cyclic voltammetry of $Fe(CN)_6^{3-/4-}$ in the thin-layer cell. (A) Effect of layer thickness (left), scan rate (middle), and $Fe(CN)_6^{3-/4-}$ concentration (right) on the representative background-corrected *i-E* curves under indicated conditions. (B) The average oxidation peak current (left; µA mM^{-1} $µm^{-1}$) and faradaic charge (middle; µC mM^{-1} $µm^{-1}$) normalized to the amount of analyte, and peak separations (right) obtained from multiple *i-E* curves for 0.25 - 1.0 mM $Fe(CN)_6^{3-/4-}$ at scan rates of 1-20 mV/s with 7.5 µm (red), 25 µm (green), and 75 µm (blue) spacers. Measurements were carried out on a glassy carbon working electrode in 1 M KCl as a supporting electrolyte.

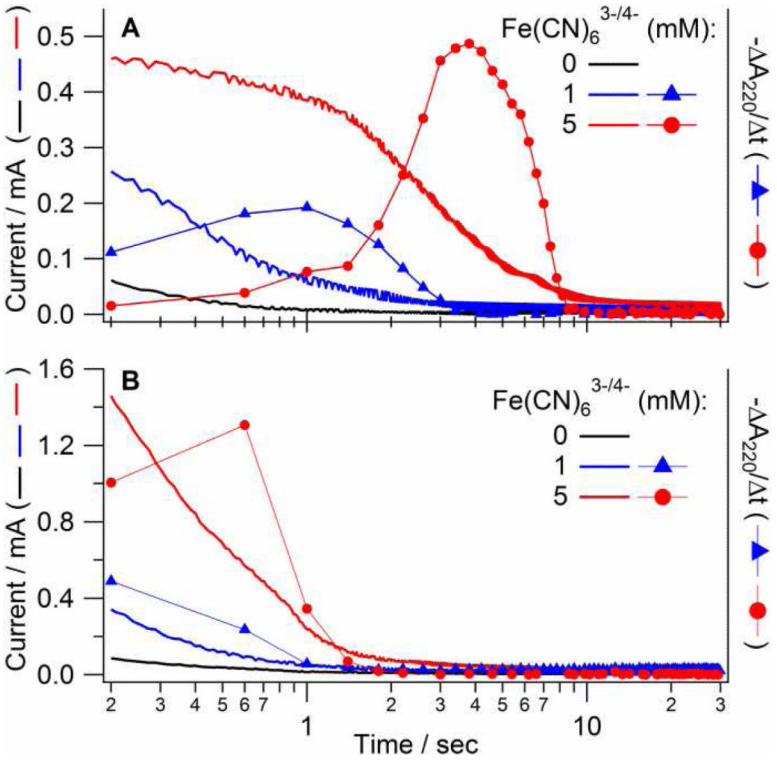

Figure 3.

Simultaneous recording of the current and optical absorption changes over time during electrochemical oxidation of $Fe(CN)_6^{4-}$ in the thin-layer cell. Reaction was initiated by a potential step from -0.1 to 0.6 V for 0, 1, or 5 mM $Fe(CN)_6^{-4}$ in 0.1 M (A) or 1 M (B) KCl on a Au-MG electrode with 25 μm spacer. Simultaneously measured current and the rate of absorption changes ($-\Delta A/\Delta t$) are shown against left and right scales, respectively. Both types of data represent the rate of electrochemical process and thus can be correlated directly. Time is shown on the logarithmic scale.

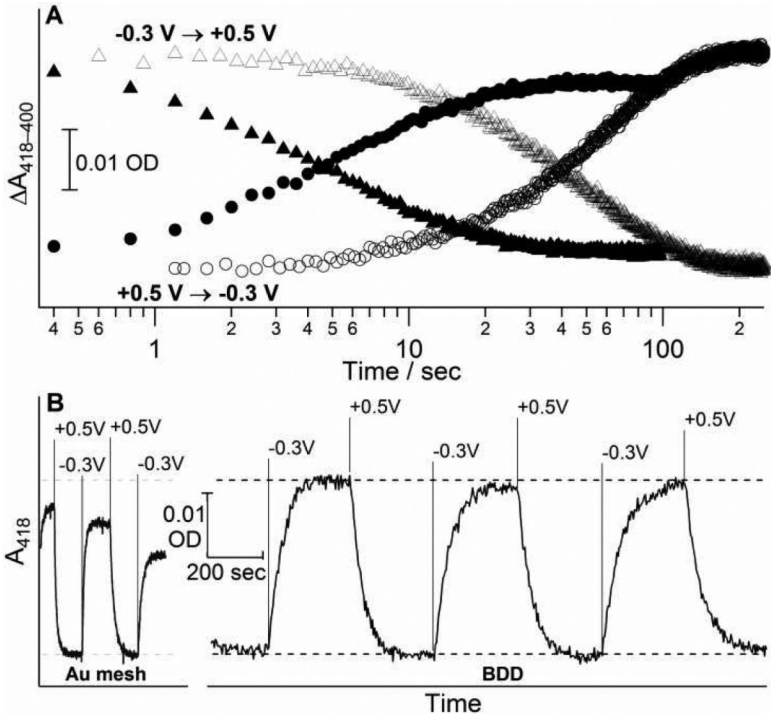

Figure 4.

Chronospectrometry of cytochrome *c* on gold minigrid and boron-doped diamond. (A) The kinetics of oxidation (triangles) and reduction (circles) of C*c* on Au-MG (closed markers) and BDD film on quartz (open markers) electrodes. (B) Reversibility of C*c* reduction/oxidation on gold minigrid (left) and boron-doped diamond film (right) upon potential steps between 0.5 V and -0.3 V at indicated times. Dashed lines show maximum amplitude of spectral changes. Sample: 0.1 mM cytochrome *c* in 10 mM phosphate buffer (pH 7), 100 mM KCl; 75 μm spacer. Time is shown on the logarithmic scale for panel A and linear scale for panel B.

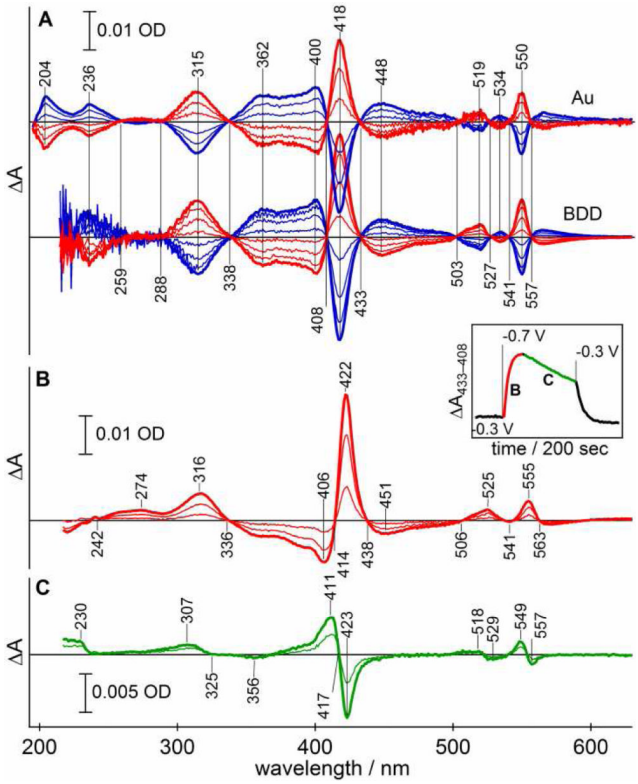

Figure 5.

UV-Vis optical spectroelectrochemical response of cytochrome *c* and its cyanide complex. (A) Difference absorption spectra of reduction (red) and oxidation (blue) of native C*c* on gold minigrid (top) and BDD (bottom). (B) Rapid optical changes observed for C*c*-CN^- complex over first 20 sec following a potential step to -0.7V on BDD after pre-incubation at -0.3 V. (C) Slower optical changes observed after the reduction of C*c*-CN^- complex shown in panel B; spectra are shown as a difference vs. fully reduced complex at 20 sec. Insert: temporal changes in optical difference between isosbestic points of the native cytochrome *c* at 433 nm and 408 nm; time periods representing spectra in panels B and C are shown. Sample: 0.1 mM cytochrome *c* in 0.1 M KCN, Tris buffer (pH 7), 100 mM KCl; 75 μm spacer.